Femtosecond laser pulse control of multidimensional vibrational dynamics: Computational studies on the pyrazine molecule

Luxia Wang[a)]
Institut für Physik, Humboldt-Universität zu Berlin, Newtonstraße 15, D-12489 Berlin, Germany

Hans-Dieter Meyer
Theoretische Chemie, Universität Heidelberg, Im Neuenheimer Feld 229, D-69120 Heidelberg, Germany

Volkhard May
Institut für Physik, Humboldt-Universität zu Berlin, Newtonstraße 15, D-12489 Berlin, Germany

(Received 21 February 2006; accepted 4 May 2006; published online 5 July 2006)

The multiconfiguration time-dependent Hartree (MCTDH) method is combined with the optimal control theory (OCT) to study femtosecond laser pulse control of multidimensional vibrational dynamics. Simulations are presented for the widely discussed three-electronic-level vibronic coupling model of pyrazine either in a three or four vibrational coordinate version. Thus, for the first time OCT is applied to a four-coordinate system. Different control tasks are investigated and also some general aspects of the OCT-MCTDH method combination are analyzed. © *2006 American Institute of Physics*. [DOI: 10.1063/1.2208611]

I. INTRODUCTION

It is of ongoing interest to explore molecular dynamics by special tailored femtosecond laser pulses (see, for example, Refs. 1 and 2). While multidimensional wave packet dynamics in polyatomic and condensed phase systems have been studied in closed loop control experiments,[3–7] simulations based on the optimal control theory (OCT) are restricted to models with at most two nuclear coordinates (for example, Refs. 8–10). However, to understand the molecular dynamics underlying the particular control mechanism realized in the experiment, more sophisticated models are often necessary.

One efficient way to treat multidimensional vibrational dynamics in molecular systems is offered by the multiconfiguration time-dependent Hartree (MCTDH) method.[11–13] In this method the wave function is expanded in a basis of time-dependent product states (Hartree products) with also time-dependent expansion coefficients. In the most basic form every wave function forming the product basis belongs to a single vibrational coordinate defining the so-called single particle functions (SPFs). This basis adapts itself to the evolving wave packet and remains optimally small, allowing larger systems to be treated efficiently.

Here, we will apply the combination of the MCTDH method with the OCT to carry out simulations for the widely studied pyrazine molecule.[14–18] For our purposes an electronic three-state model complemented by three or four vibrational modes is sufficient. Besides the S_0 ground state, it covers the excited $S_1(\pi,\pi^*)$ and $S_2(n,\pi^*)$ states, where the latter are vibrationally coupled and exhibit a conical intersection.

The respective Hamiltonian used for our simulations is shortly recalled in Sec. II. Afterwards, the combination of the MCTDH method with the OCT is introduced in Sec. III. In Sec. IV numerous numerical results are presented, and the paper ends with some concluding remarks in Sec. V.

II. THE MODEL

The three-electronic-state vibronic coupling model of pyrazine has been described at various places in literature (see, e.g., Refs. 14–18). Here, we only recall some basic features. The overall pyrazine Hamiltonian including the coupling to the radiation field is written as

$$H(t) = H_{\mathrm{mol}} + H_{\mathrm{field}}(t). \tag{1}$$

The molecular part expanded in a diabatic basis reads[19,20]

$$H_{\mathrm{mol}} = H_{\mathrm{vib}}|\varphi_{S_0}\rangle\langle\varphi_{S_0}| + \sum_{a=S_1,S_2}\left(E_a + H_{\mathrm{vib}} + \sum_{j\in\Gamma_1}\kappa_j^{(a)}Q_j\right) \times|\varphi_a\rangle\langle\varphi_a| + \sum_{j\in\Gamma_3}(\lambda_j Q_j|\varphi_{S_1}\rangle\langle\varphi_{S_2}| + \mathrm{H.c.}), \tag{2}$$

where φ_a denotes the electronic wave function of state a ($a=S_1,S_2$), the E_a are the vertical electronic excitation energies (note that E_{S_0} has been set equal to zero), and the vibrational Hamiltonian is given by

$$H_{\mathrm{vib}} = \sum_j \frac{\hbar\omega_j}{2}\left(-\frac{\partial^2}{\partial Q_j^2} + Q_j^2\right). \tag{3}$$

In H_{mol}, Eq. (2), Γ_1 indicates the set of totally symmetric modes and Γ_3 corresponds to the set of asymmetric ones which provide a linear coupling between the two excited states.[14,17,19–21] In the following we use a description with the single nontotally symmetric coupling mode $j=10a$ (out of plane vibration) and two or three totally symmetric tuning modes $j=1,6a$ or $j=1,6a,9a$ (ring stretching and bending vibrations), respectively. All parameters for the three- and four-mode models of pyrazine are listed in Table I. For fur-

a)Electronic mail: luxia@physik.hu-berlin.de

TABLE I. Parameters of the three-electronic-state vibronic coupling model for pyrazine [see Eq. (2)] based either on three (Refs. 15 and 17) or four vibrational modes (Refs. 19 and 20). The oscillation periods T_j of the vibrational modes and their equilibrium positions $Q_j^{(a)}$ in the two excited states are also given ($\hbar\omega_j$, $\kappa_j^{(S_1)}$, $\kappa_j^{(S_2)}$ and λ_j in eV, T_j in fs). The vertical electronic excitation energies amount to E_{S_1}=3.94 eV and E_{S_2}=4.84 eV.

j	$\hbar\omega_j$	$\kappa_j^{(S_1)}$	$\kappa_j^{(S_2)}$	λ_j	T_j	$Q_j^{(S_1)}$	$Q_j^{(S_2)}$
1	0.126	0.037	−0.254	⋯	32.8	−0.29	2.02
6*a*	0.074	−0.105	0.149	⋯	55.9	1.42	−2.01
10*a*	0.118	⋯	⋯	0.262	35.0	0	0
1	0.127	0.047	0.201	⋯	32.5	−0.37	−1.58
6*a*	0.074	−0.096	0.119	⋯	55.9	1.30	−1.61
9*a*	0.157	0.159	0.048	⋯	26.3	−1.02	−0.31
10*a*	0.094	⋯	⋯	0.183	44.2	0	0

ther use it also contains the oscillation periods T_j of the vibrational modes and their equilibrium positions $Q_j^{(a)}$ in the two excited states.

In pyrazine the $S_0-S_1(\pi\pi^*)$ and S_0-$S_2(n\pi^*)$ transitions are dipole allowed, whereas the S_1-S_2 transition is dipole forbidden. The oscillator strength of the S_0-S_1 transition, however, is approximately ten times smaller than that of the S_0-S_2 transition and, therefore, will be neglected in what follows (some test calculations confirmed this decision). Consequently, the coupling to the radiation field is written as

$$H_{\text{field}}(t) = -\mathbf{E}(t)\hat{\mu} \equiv -\mathbf{E}(t)(\mathbf{d}|\varphi_{S_2}\rangle\langle\varphi_{S_0}| + \text{H.c.}). \tag{4}$$

The transition-dipole matrix element is denoted by $\mathbf{d}$ and is assumed to be independent of the nuclear coordinates (Condon approximation). The electric field strength $\mathbf{E}$ should be linearly polarized (the polarization unit vector is $\mathbf{n}$).

In the following we will restrict the discussion to intramolecular electronic and vibrational dynamics. Thus, any coupling of the excited molecules to an environment (in the condensed phase) or to their rotational motion (in the gas phase) has been neglected. The effect of a possible random spatial orientation of the molecules is also suppressed (the product of $\mathbf{d}$ and of the field polarization $\mathbf{n}$ is fixed and identical for all molecules). And a low temperature situation is considered. Consequently, the ensemble of molecules can be represented by a pure state before excitation, i.e., by the vibrational ground state of the electronic ground state and a fixed spatial orientation.

III. OPTIMAL CONTROL SCHEME COMBINED WITH THE MCTDH METHOD

In its standard version laser pulse control of molecular dynamics is formulated as the task to maximize an observable O at a particular final time t_f by radiation field excitation.[22–25] In the present case of pure-state dynamics the observable is obtained as

$$O(t_f;\mathbf{E}) = \langle\Psi(t_f)|\hat{O}|\Psi(t_f)\rangle, \tag{5}$$

where $\hat{O}$ is the operator corresponding to the observable and $\Psi(t_f)$ denotes the laser pulse driven system wave function at final time t_f (for simplicity, the notation neglects the dependence of all wave functions on $\mathbf{E}$). Assuming a single state Ψ_{tar} which should be reached at t_f (target state), $\hat{O}$ would become the projector $|\Psi_{\text{tar}}\rangle\langle\Psi_{\text{tar}}|$.

The maximization of $O(t_f)$ is achieved by applying the OCT based on the functional

$$J(t_f;\mathbf{E}) = O(t_f;\mathbf{E}) - \tfrac{1}{2}\int_{t_0}^{t_f} dt\lambda(t)\mathbf{E}^2(t). \tag{6}$$

This so-called *control functional* contains a constraint to guarantee finite field intensity, where the respective Lagrange parameter $\lambda(t)$ includes a time dependence $\lambda(t) = \lambda_0/\sin^2(\pi t/t_f)$ to switch the laser field on and off smoothly.[8]

In searching for the extremum of $J(t_f;\mathbf{E})$ the laser pulse can be calculated which solves the control task. It is usually named *optimal pulse* and the respective value of $O(t_f;\mathbf{E})$ is known as the *control yield*. The optimal pulse has to be deduced from the following functional equation:

$$\mathbf{E}(t) = -\frac{2}{\hbar\lambda(t)}\,\text{Im}\langle\Theta(t)|\hat{\mu}|\Psi(t)\rangle, \tag{7}$$

where the wave function $\Psi(t)$ obeys the standard time-dependent Schrödinger equation (including the laser pulse and with the initial value $|\Psi_0\rangle$)

$$i\hbar\frac{\partial}{\partial t}|\Psi(t)\rangle = (H_{\text{mol}} - \mathbf{E}(t)\hat{\mu})|\Psi(t)\rangle. \tag{8}$$

The function $\Theta(t)$ results from a similar equation,

$$i\hbar\frac{\partial}{\partial t}|\Theta(t)\rangle = (H_{\text{mol}} - \mathbf{E}(t)\hat{\mu})|\Theta(t)\rangle, \tag{9}$$

but propagated backwards in time starting at t_f and ending at t_0. The respective "initial" value reads

$$|\Theta(t_f)\rangle = \hat{O}|\Psi(t_f)\rangle. \tag{10}$$

In Refs. 26 and 27 an iteration scheme to determine the optimal pulse has been suggested which combines these forward and backward propagations iteratively. The key point in this connection is the replacement of the field strength in Eqs. (8) and (9) by the right-hand side of Eq. (7), resulting in coupled nonlinear Schrödinger equations for forward and backward propagations. When iterating these equations one guesses an initial pulse $\mathbf{E}^{(0)}(t)$ to compute the zeroth-order wave function $\Psi^{(0)}(t)$ using directly Eq. (8). For the subse-

quent backward propagation (calculation of $\Theta^{(0)}$) one replaces $\mathbf{E}(t)$ in Eq. (9) by $-2\,\mathrm{Im}\langle\Theta^{(0)}(t)|\hat{\mu}|\Psi^{(0)}(t)\rangle/(\hbar\lambda(t))$ according to Eq. (7). The nonlinear Schrödinger equation for $\Theta^{(0)}$ can be solved and the whole procedure is extended up to the case that convergence is obtained. The nth forward iteration uses the result of the $(n-1)$th backward iteration and the nth backward iteration uses the result of the nth forward iteration. Within every iteration step (finalized after the computation of $\Psi^{(n)}$) an approximate optimal pulse $\mathbf{E}^{(n)}(t)$ can be calculated from the right-hand side of Eq. (7). Different authors demonstrated that this iteration scheme exhibits quadratic and monotonic convergence (see Refs. [27–29]).

It is the specialty of the approach presented here that the time dependence of the state vectors $|\Psi\rangle$ as well as $|\Theta\rangle$ are determined by the MCTDH method.[11–13] In order to apply the MCTDH method one introduces an expansion with respect to the diabatic electronic states ($a=S_0,S_1,S_2$):

$$|\Psi(t)\rangle=\sum_a \chi_a(Q,t)|\varphi_a\rangle, \tag{11}$$

and

$$|\Theta(t)\rangle=\sum_a \vartheta_a(Q,t)|\varphi_a\rangle, \tag{12}$$

resulting in vibrational wave functions $\chi_a(Q,t)$ and $\vartheta_a(Q,t)$ for the forward and the backward propagation, respectively. As already mentioned the initial wave function for the forward propagation is given by the vibrational ground state of the S_0 level. The initial values for the ϑ functions follow from Eq. (10) as

$$|\vartheta_a(t_f)\rangle=\sum_b \langle\varphi_a|\hat{O}|\varphi_b\rangle|\chi_b(t_f)\rangle. \tag{13}$$

The expansion with respect to the electronic states transforms Eq. (7) for the optimal pulse into the following form [see also Eq. (4)]:

$$\mathbf{dE}(t)=-\hbar\Lambda_0\sin^2\left(\frac{\pi t}{t_f}\right)\mathrm{Im}(\langle\vartheta_{S_2}(t)|\chi_{S_0}(t)\rangle + \langle\vartheta_{S_0}(t)|\chi_{S_2}(t)\rangle). \tag{14}$$

The expression is written using the Rabi energy $\mathbf{dE}(t)$ the introduction of which is appropriate for the numerical calculations. Moreover, $1/\lambda_0$ has been replaced by the effective parameter $\Lambda_0=2|\mathbf{d}|^2/(\hbar^2\lambda_0)$ (notice that $\hbar\Lambda_0$ has the dimension of energy). Although the functions χ_{S_1} and ϑ_{S_1} do not appear in the expression determining the optimal pulse, of course, they enter the set of coupled wave equations.

The time-dependent Schrödinger equations for the vibrational wave functions χ_a and ϑ_b are solved within the MCTDH method[13] by introducing the following expansion (shown here for χ_a):

$$\chi_a(Q,t)=\sum_{\kappa_1=1}^{M_1}\sum_{\kappa_2=1}^{M_2}\cdots\sum_{\kappa_N=1}^{M_N}A^{(a)}_{\kappa_1\kappa_2\cdots\kappa_N}(t)\prod_{j=1}^{N}\zeta^{(a)}_{\kappa_j}(Q_j,t). \tag{15}$$

The quantity M_j is the number of single particle functions $\zeta^{(a)}_{\kappa_j}(Q_j,t)$ for mode j $(=1,\ldots,N)$ and the $A^{(a)}_{\kappa_1\kappa_2\cdots\kappa_N}(t)$ are the time-dependent expansion coefficients for the particular Hartree products $\Pi_j\zeta^{(a)}_{\kappa_j}(Q_j,t)$. The expansion coefficients as well as the Hartree products additionally depend on the electronic quantum number $a=S_0,S_1,S_2$. The wave functions $\vartheta_a(Q,t)$ of the backward propagation have to be expanded in the same way.

As detailed, for example, in Ref. 13 the ansatz [Eq. (15)] on which the MCTDH method is based on, results in coupled nonlinear equations of motion for the single particle functions and the expansion coefficients. At the moment it cannot be proven if these equations of motion also result in a quadratic and monotonic convergence as it is the case for the iteration scheme mention beforehand to determine the optimal pulse. Such an iteration scheme, however, is also not applicable within the existing MCTDH code.[30] This is because the code does not allow for the solution of time-dependent Schrödinger equations which become nonlinear like those obtained via a replacement of the field strength by the expression given in Eq. (7). Therefore, it only remains to prove convergence within the course of the numerical calculations.

To remain sufficiently close to the original iteration we did not approximate the field strength $\mathbf{E}^{(n)}(t)$ of the actual iteration (which enters the equations for the $\chi^{(n)}_a$ and $\vartheta^{(n)}_b$) by the field strength of the foregoing iteration. Instead, values calculated at earlier times but within the same iteration are used to obtain $\mathbf{E}^{(n)}(t)$ via a quadratic extrapolation. Consequently, to get the nth iteration of the field at times t and $t+\Delta t$, first, the field at the preceding time $t-\Delta t$ is computed according to

$$\mathbf{E}^{(n)}(t-\Delta t)=-\frac{2}{\hbar\lambda(t-\Delta t)}\times\mathrm{Im}\langle\Theta^{(n-1)}(t-\Delta t)|\hat{\mu}|\Psi^{(n)}(t-\Delta t)\rangle. \tag{16}$$

This expression uses the function Θ (or the functions ϑ_b) of the foregoing iteration and the function Ψ (or the functions χ_a) of the present iteration but determined in the foregoing time step. To carry out the extrapolation two auxiliary fields have to be introduced, namely,

$$\mathbf{E}^{(1)}_{\mathrm{aux}}=\tfrac{1}{2}(\mathbf{E}^{(n)}(t-3\Delta t)-4\mathbf{E}^{(n)}(t-2\Delta t)+3\mathbf{E}^{(n)}(t-\Delta t)), \tag{17}$$

and

$$\mathbf{E}^{(2)}_{\mathrm{aux}}=\tfrac{1}{2}(\mathbf{E}^{(n)}(t-3\Delta t)-2\mathbf{E}^{(n)}(t-2\Delta t)+\mathbf{E}^{(n)}(t-\Delta t)), \tag{18}$$

resulting in extrapolated field strengths

$$\mathbf{E}^{(n)}(t)=\mathbf{E}^{(n)}(t-\Delta t)+\mathbf{E}^{(1)}_{\mathrm{aux}}+\mathbf{E}^{(2)}_{\mathrm{aux}}, \tag{19}$$

and

$$\mathbf{E}^{(n)}(t+\Delta t)=\mathbf{E}^{(n)}(t-\Delta t)+2\mathbf{E}^{(1)}_{\mathrm{aux}}+4\mathbf{E}^{(2)}_{\mathrm{aux}}. \tag{20}$$

Note that these two extrapolated field strengths together with $\mathbf{E}^{(n)}(t-\Delta t)$ are necessary for the whole application of the MCTDH code. Some illustrative examples indicating the numerically stable convergence behavior of this iteration scheme can be found in Appendix B.

IV. NUMERICAL RESULTS

To present data on the application of the combined OCT-MCTDH method we first concentrate on the control yield which is given by $O(t_f;\mathbf{E})$, Eq. (5), calculated with the optimal pulse. But we will also analyze the overall electronic state populations obtained as

$$P_a(t) = \langle \chi_a(t) | \chi_a(t) \rangle \equiv \int dQ |\chi_a(Q,t)|^2, \tag{21}$$

where Q abbreviates the whole set of coordinates and $\int dQ$ the respective integration. Furthermore, to characterize the laser pulse driven vibrational dynamics in more detail reduced single-coordinate probability distribution functions referring to a particular electronic state are introduced. When focused on the vibrational coordinate Q_j they read

$$p_a(Q_j,t) = \int d\tilde{Q} |\chi_a(Q,t)|^2, \tag{22}$$

where $\int d\tilde{Q}$ indicates that the integration has to be taken with respect to all coordinates except Q_j. In Appendix A we present both quantities, Eqs. (21) and (22), for a wave packet moving freely (without external field control) between the S_2 and S_1 states after an impulsive excitation into the S_2 state. This should serve as a reference case for all subsequent studies on laser pulse driven dynamics.

As a third observable we will compute the coordinate expectation value referring to electronic state φ_a which is defined as

$$\langle Q_j^{(a)}(t) \rangle \equiv \langle \chi_a(t) | Q_j | \chi_a(t) \rangle = \int dQ_j Q_j p_a(Q_j,t). \tag{23}$$

Details on the performance of the combined OCT-MCTDH method are given in Appendix B. Notice that for all data presented in the following 15 iterations have been sufficient to arrive at rather well converged results (see also Appendix B).

A. Reference calculations: Neglect of the S_1 State

We start our considerations in neglecting the vibronic coupling among the two excited electronic states just considering the excitation of the S_2 state only. This will be done in exclusively using the three-mode model of pyrazine. Although somewhat artificial when considering pyrazine these computations serve as a reference case for later investigations. In particular, they will demonstrate to what extent a vibrational wave packet in the excited S_2-state potential energy surface (PES) may be prepared.

First, for the sake of simplicity, let us assume that the target state is the whole electronic state S_2, without any dependency on a particular vibrational state. Then, we have to set $\hat{O} = |\varphi_{S_2}\rangle\langle\varphi_{S_2}|$ and the control yield follows as $O(t_f;\mathbf{E}) = P_{S_2}(t_f)$, Eq. (21), with $t_f = 100$ fs. It can be seen in Fig. 1 that the optimal laser pulse covers about one-half of the whole time interval, it starts to excite the system at about 20 fs; the amplitude of the-field increases with time, gets its maximum at about 60 fs, and switches off at about 80 fs. The shape of the field differs from a simple Gaussian, and the control yield can become as large as 0.95 (here we use $\hbar\Lambda_0 = 2$ eV).

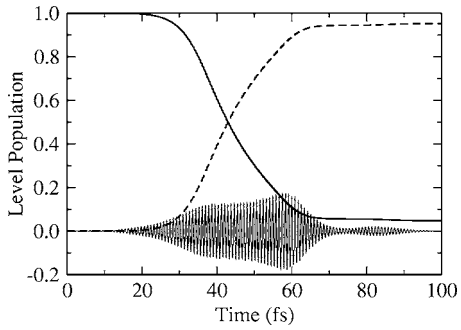

FIG. 1. Laser pulse control of pyrazine described by a three-mode two-electronic-state model. Solid line: S_0-state population; dashed line: S_2-state population, lower part of the figure: temporal behavior of the optimal pulse field strength. The target state of the control task is given by the complete S_2 state to be reached at $t_f = 100$ fs (the unit 0.1 at the axis corresponds to an electric field strength of about 2×10^7 V/cm).

Since the vibronic coupling is switched off in this example, the coordinate probability distribution, Eq. (22), of the coupling mode Q_{10a} does not display any oscillation (not shown). On the contrary, the probability distributions of both tuning modes oscillate around their S_2-state equilibrium positions (see Table I). Although the described control task is a simple attempt to maximize the population of a parabolic PES in a three-dimensional coordinate space details of the dynamics appear less trivial. In particular, the optimal pulse deviates from a simple Gaussian one. Apparently, this is caused by the motion of a wave packet accompanying the excitation of the electronic state. But the results also indicate the complex behavior of the wave function defined versus three coordinates in a rather simple control task.

The foregoing considerations are continued by using a particular vibrational wave packet in the S_2 state as the target, i.e., we set $|\Psi_{\text{tar}}\rangle = \chi^{(\text{tar})}(Q)|\varphi_{S_2}\rangle$. The vibrational target wave function $\chi^{(\text{tar})}(Q)$ is chosen as the wave function of the vibrational ground state in the electronic ground-state PES, given by $\Pi_j \chi_{S_0,0}(Q_j)$, but displaced by $Q_j^{(\text{tar})}$ fixing the posi-

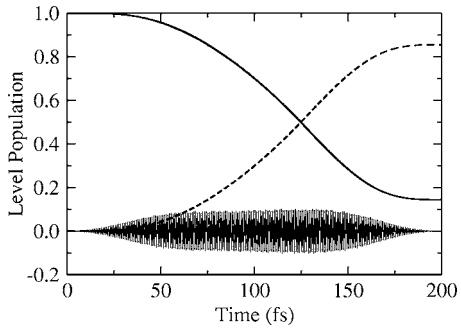

FIG. 2. Laser pulse control of pyrazine described by a three-mode two-electronic-state model. Solid line: S_0-state population, dashed line: S_2-state population, lower part of the figure: temporal behavior of the optimal pulse field strength. The target state of the control task should be reached at $t_f = 200$ fs and is given by a vibrational state in the S_2 state following from the vibrational ground-state function displaced into the S_2-state equilibrium position (the unit 0.1 at the axis corresponds to an electric field strength of about 2×10^7 V/cm).

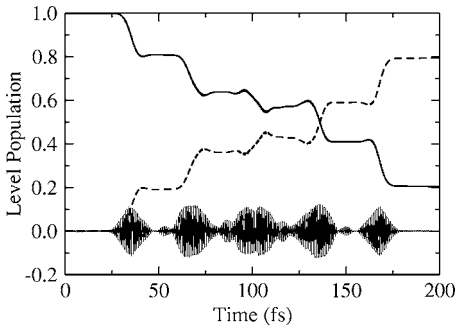

FIG. 3. Laser pulse control of pyrazine described by a three-mode two-electronic-state model. Solid line: S_0-state population, dashed line: S_2-state population, lower part of the figure: temporal behavior of the optimal pulse field strength. The target state of the control task should be reached at t_f =200 fs and is given by a vibrational state in the S_2 state following from the vibrational ground-state function displaced into $(Q_1^{(\mathrm{tar})}, Q_{6a}^{(\mathrm{tar})}, Q_{10a}^{(\mathrm{tar})})=(0.0, -2.01, 0.0)$ (the unit 0.1 at the axis corresponds to an electric field strength of 2×10^7 V/cm).

tion of the target wave packet in the excited-state PES. The related control yield reads $O(t_f;\mathbf{E})=|\langle\chi^{(\mathrm{tar})}|\chi_{S_2}(t_f)\rangle|^2$.

The approach described so far aims at a complete match of the target state. However, for target vibrational states positioned in an excited electronic state it would be also reasonable to maximize the overlap of the driven wave function with the target wave function but at an overall excited state population much less than 1. This is typical for a weak-field situation where the excited wave function solves the control task but with a very small overall excitation. Arriving at lower control yields in the following is such a possibility that has to be taken into consideration. Therefore the renormalized control yield $O^{(\mathrm{ren})}(t_f;\mathbf{E})=O(t_f;\mathbf{E})/P_{S_2}(t_f)$ is introduced.

The reference example among such target states is the one where $\chi^{(\mathrm{tar})}(Q)$ is centered at the equilibrium position of the S_2 state, i.e., it is described by the displaced vibrational

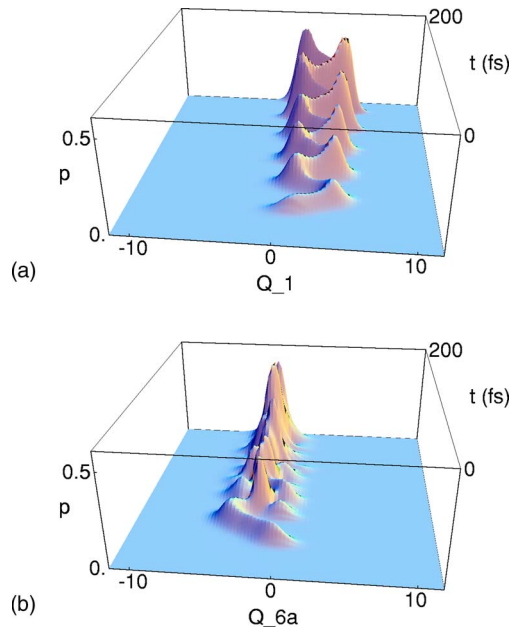

FIG. 4. Temporal evolution of the reduced S_2-state coordinate probability distributions referring to the control task of Fig. 3. Upper panel: mode 1 and lower panel: mode $6a$.

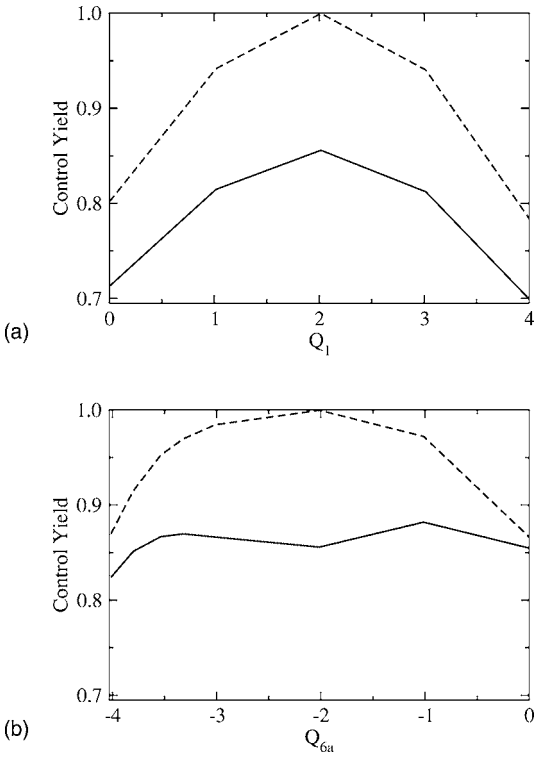

FIG. 5. Control yield for a laser pulse driven vibrational wave packet motion into vibrational states displaced with respect to either the Q_1 or the Q_{6a} coordinate. The upper panel shows the yield vs the target wave packet position along the Q_1 coordinate and the lower panel the yield vs the Q_{6a} coordinate. In any case the wave packet position with respect to the two other coordinates is given by the S_2-state equilibrium position. The solid line gives the overall control yield and the dashed line the renormalized yield (see also text).

ground states $\Pi_j\chi_{S_0,0}(Q_j-Q_j^{(\mathrm{tar})})$, where the $Q_j^{(\mathrm{tar})}$ specify the displacement, here taken as $Q_j^{(\mathrm{tar})}=Q_j^{(S_2)}$ (see Table I). In order to ensure that the laser pulse induced vibrational wave packet excitation and driving becomes efficient enough we put t_f at 200 fs. Figure 2 shows the electronic state populations P_{S_0} and P_{S_2}, together with the optimal pulse. The much higher specialty of the target state compared with the case shown in Fig. 1 leads to a decrease of the control yield (0.85 instead of 0.95).

In a further step we place the target wave packet to a position where one tuning mode is displaced from its vibrational equilibrium position. Figure 3 shows the related overall electronic state populations and the optimal pulse covering five well separated subpulses. They result in a stepwise change of the level populations and are in phase with the oscillating excited state vibrational wave packet. The behavior of the latter is displayed in Fig. 4. However, while a strong oscillation can be observed with respect to the Q_1-probability distribution resulting in the maximal value at $Q_1=0$ at t_f, the other tuning mode starts to oscillate but later its motion is damped to arrive at $Q_{6a}=Q_{6a}^{(\mathrm{tar})}$ at $t=t_f$. In contrast, the Q_{10a} probability monotonously increases up to the final time t_f (not shown).

The computations presented so far are finalized by an investigation of similar control tasks with a series of systematically displaced vibrational target states in the electronic excited state. The upper panel of Fig. 5 shows the control

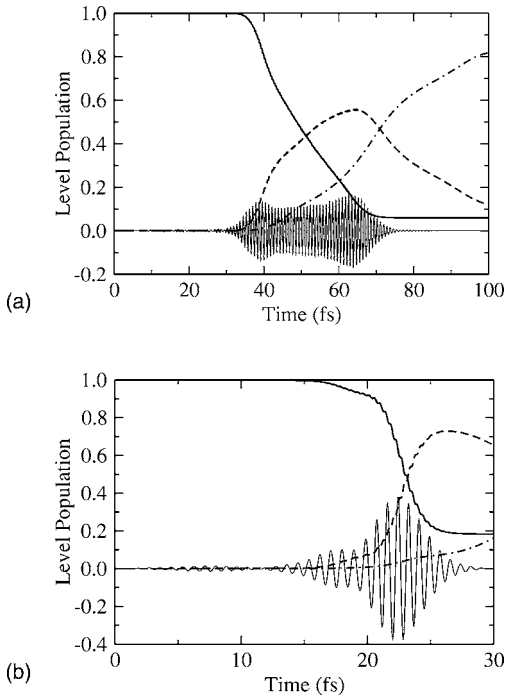

FIG. 6. Laser pulse controlled maximization of the overall S_1-state population (upper panel, $t_f=100$ fs) and of the S_2-state population (lower panel, $t_f=30$ fs). Solid line: S_0-state population, dashed line: S_2-state population, dashed-dotted line: S_1-state population, thin solid line: temporal behavior of the respective optimal pulse (the unit 0.1 at the axis corresponds to an electric field strength of about 2×10^7 V/cm).

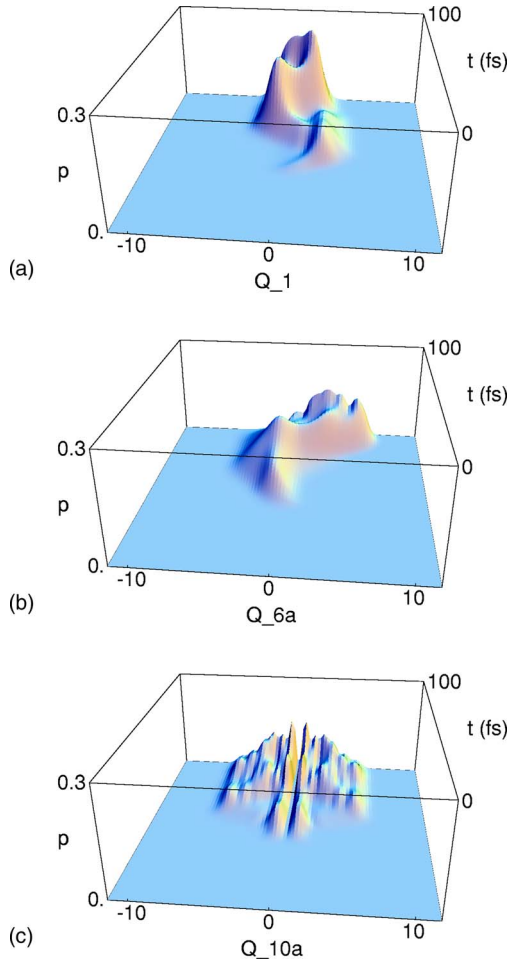

FIG. 7. Temporal evolution of the reduced S_1-state coordinate probability distributions referring to the control task of the upper panel of Fig. 6. From the top to the bottom: mode 1, mode 6*a*, and mode 10*a*.

yield versus the location of the target wave packet at the Q_1 coordinate. The center of the wave packet with respect to the 6*a* and 10*a* modes is fixed at their equilibrium position. Similar results but now with the control yield versus the location of the target wave packet at the Q_{6a} coordinate are shown in the lower panel of Fig. 5. To make the results of this series of OCT solutions comparable we also present the renormalized control yield $O^{(\mathrm{ren})}$ obtained by taking the ratio of the control yield and the overall population of the S_2 state. The latter quantity gets its maximum value of 1 at the respective equilibrium position of the S_2-state PES. While the control yield versus the Q_1-coordinate wave packet location is rather symmetric with respect to the equilibrium position this is not the case when drawing similar data versus the Q_{6a}-coordinate (see lower panel of Fig. 5). Moreover, one notices that the control yield is more influenced by a displacement with respect to the Q_1 coordinate than with respect to the Q_{6a} coordinate, which is caused by the smaller vibrational frequency of the latter mode.

B. The coupling between the S_1 and the S_2 state: Acceleration versus suppression of S_2-S_1 internal conversion

According to the computations of Refs. 16 and 31 the S_2-S_1 state conical intersection is located close to the minimum of the S_2-state PES. As a result optical excitation of the S_2 state is followed by ultrafast internal conversion (IC) into the S_1 state. Since the vibrational states of the S_2 state have a short lifetime, we can expect that laser pulse control of vibrational wave packet motion in the S_1-state PES is easy to be achieved, which, however, should be not the case for a positioning of the vibrational wave packet at the S_2 state. To compare such types of control tasks the whole S_1 or S_2 state is used to construct the target operator, i.e., we will set $\hat{O}=|\varphi_{S_1}\rangle\langle\varphi_{S_1}|$ or $\hat{O}=|\varphi_{S_2}\rangle\langle\varphi_{S_2}|$. The final time t_f at which the target state should be reached is taken as 100 fs as well as 30 fs where the latter value is dictated by the fast S_2-S_1 transition taking place within some 10 fs; moreover, we set $\hbar\Lambda_0=2$ eV.

TABLE II. Control yield $O(t_f;\mathbf{E})$ and renormalized yield $O^{(\mathrm{ren})}(t_f;\mathbf{E})$ obtained within the control tasks described in Sec. IV C. The results are ordered with respect to the target state specified by the electronic level and the localization of the coupling mode vibrational wave packet. A second set of results, where the position of the target state on the coupling mode has been changed, are also tabularized and are listed in parentheses. The wave packets in the tuning modes are localized at the equilibrium position in their respective electronic states. The final time t_f and the parameter Λ_0 are also given (for details see text).

Target state	t_f (fs)	$\hbar\Lambda_0$ (eV)	$O(t_f;\mathbf{E})$	$O^{(\mathrm{ren})}(t_f;\mathbf{E})$
S_1;1.0(2.0)	100	10	0.197(0.315)	0.310(0.462)
S_1;1.0(2.0)	200	10	0.251(0.361)	0.306(0.459)
S_1;1.0(2.0)	400	10	0.260(0.373)	0.301(0.465)
S_0;1.0(2.0)	200	10	0.384(0.311)	0.414(0.336)
S_2;1.0	100	10	0.134	0.243

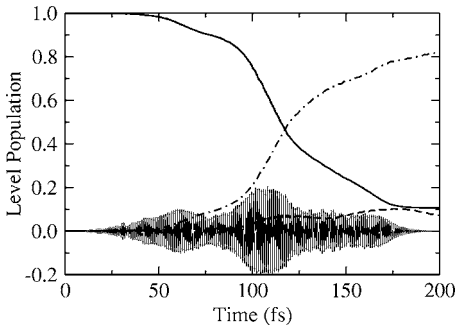

FIG. 8. Laser pulse controlled wave packet formation in the S_1 state with the target wave packet located at $(Q_1^{(\mathrm{tar})},Q_{6a}^{(\mathrm{tar})},Q_{10a}^{(\mathrm{tar})})=(-0.29,1.42,1.0)$. Solid line: S_0-state population, dashed line: S_2-state population, dashed-dotted line: S_1-state population, thin solid line: temporal behavior of the respective optimal pulse (the unit 0.1 at the axis corresponds to an electric field strength of 2×10^7 V/cm).

A comparison of the S_0-, S_1-, and S_2-level populations as well as the shape of the optimal pulse are presented in Fig. 6. The upper panel of Fig. 6 demonstrates the temporal behavior of all electronic level populations if the target states are given by the S_1 level. The necessary intermediate S_2-level population and the fast IC result in a rather high control yield. For the reverse case with the S_2 state as the target state (lower panel of Fig. 6) we reduced t_f to 30 fs. Otherwise, OCT would displace the optimal pulse to start to act at about 85 fs and to reach the target at 100 fs. Now, the S_2-state (the target state) population reaches the value of 0.65, i.e., a short intermediate stabilization of the S_2-state population would be possible. But it is immediately followed by IC into the S_1 state. A neglect of the control pulse envelope function $\sin^{-2}(\pi t/t_f)$ introduced in Eq. (14) allows the optimal pulse to reach larger values in the close vicinity of t_f with a larger control yield. However, a somewhat longer laser pulse driven stabilization of S_2-state population becomes impossible. This all indicates that within the given scheme of OCT a pronounced suppression of IC is impossible.

Additionally, this conclusion is illustrated in Fig. 7 showing the temporal behavior of the three reduced coordinate probability distributions, Eq. (22), projected on the S_1 electronic target state. As shown in Fig. 7 the probability distributions of the two tuning modes Q_1 and Q_{6a} indicate an

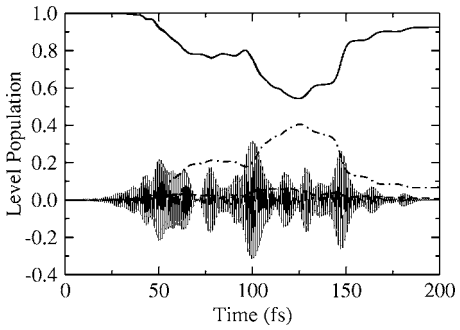

FIG. 9. Laser pulse controlled wave packet formation in the S_0 state with the target wave packet located at $(Q_1^{(\mathrm{tar})},Q_{6a}^{(\mathrm{tar})},Q_{10a}^{(\mathrm{tar})})=(-0.29,1.42,2.0)$. Solid line: S_0-state population, dashed line: S_2-state population, dashed-dotted line: S_1-state population, thin solid line: temporal behavior of the respective optimal pulse (the unit 0.1 at the axis corresponds to an electric field strength of about 2×10^7 V/cm).

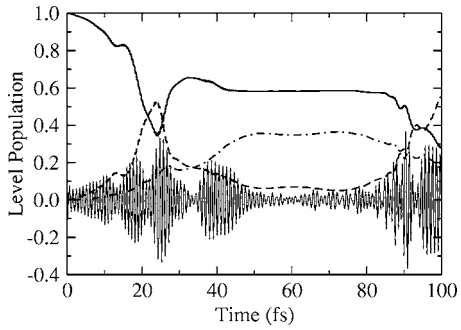

FIG. 10. Laser pulse controlled wave packet formation in the S_2 state with the target wave packet located at $(Q_1^{(\mathrm{tar})},Q_{6a}^{(\mathrm{tar})},Q_{10a}^{(\mathrm{tar})})=(2.02,-2.01,1.0)$. Solid line: S_0-state population, dashed line: S_2-state population, dashed-dotted line: S_1-state population, thin solid line: temporal behavior of the respective optimal pulse [note the absence of any time dependence of $\lambda(t)$; the unit 0.1 at the axis corresponds to an electric field strength of about 2×10^7 V/cm].

opposite oscillation of the respective wave packets. At the same time the coupling mode wave packet disperses symmetrically around its equilibrium position at $Q_{10a}^{(S_1)}=0$ with the related coordinate expectation value $<Q_{10a}^{(S_1)}(t)>$ [see Eq. (23)] also remaining at 0. This behavior gives an interesting insight into the manner the coupling mode supports the IC process.

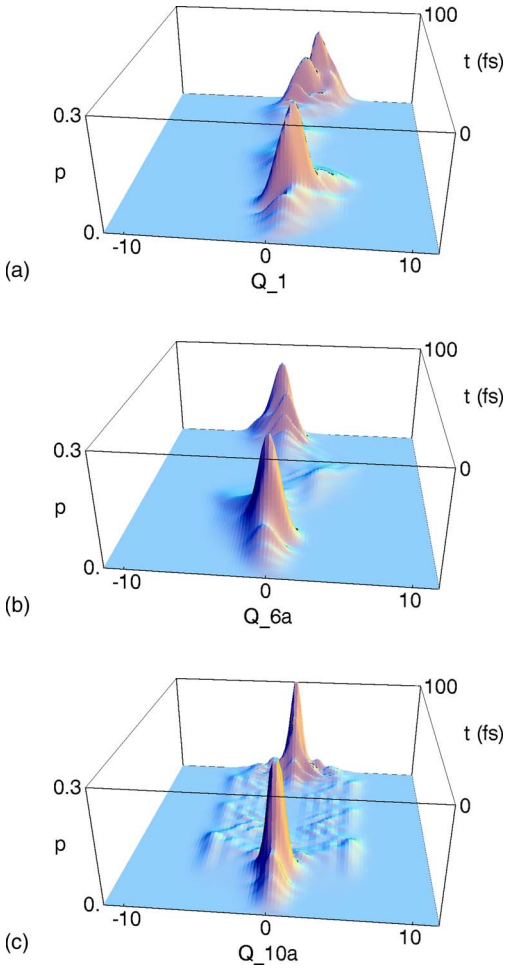

FIG. 11. Temporal evolution of the reduced S_2-state coordinate probability distributions referring to the control task of Fig. 10. From the top to the bottom: mode 1, mode $6a$, and mode $10a$.

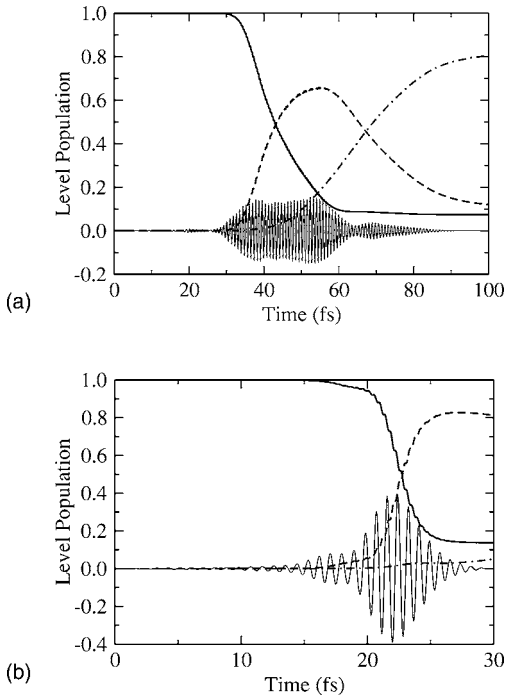

FIG. 12. Laser pulse controlled maximization of the overall S_1-state population (upper panel, t_f=100 fs) and the S_2-state population (lower panel, t_f =30 fs) using the four-coordinate model. Solid line: S_0-state population, dashed line: S_2-state population, dashed dotted line: S_1-state population, thin solid line: temporal behavior of the respective optimal pulse (the unit 0.1 at the axis corresponds to an electric field strength of 2×10^7 V/cm).

If the whole S_2 state is taken as the target state, however, the wave packet motion differs strongly from the foregoing case. At the end of the 30 fs control pulse a wave packet is excited which remains rather localized in all the vibrational coordinates (since the respective shape of the probability distributions is quite simple and looks similar in each coordinate, we did not present them here). In particular, the probability distribution related to the coupling mode does not show the broad dispersion indicating the way the optimal pulse suppresses IC. Again, this only becomes possible on a very short time interval.

To judge the obtained effect of laser pulse control we compare the presented data with the wave packet dynamics after an impulse S_2-state excitation (instantaneous vertical placement of the ground-state vibrational wave function from the S_0 into the S_2 state). The wave packet dynamics are known from literature (see Ref. 32 and references therein), but for convenience they are presented again in Appendix A. While in the undriven case the wave packet moves between the S_2 and S_1 states with a period of about 80 fs including some overtones (shorter modulations of the electronic state populations) these overtones are absent in the case of field driven dynamics of Fig. 6. And the driven dynamics avoid large S_2-state population (upper panel of Fig. 6) as well as suppress S_1-state population over a period of about 15 fs (note also the different shapes of the coordinate probability distributions). Nevertheless, for the present choice of the control task the ability of a flexible control in comparison with a free evolution of the wave packet is not so large. A more specific target state, however, will overcome this somewhat disappointing result.

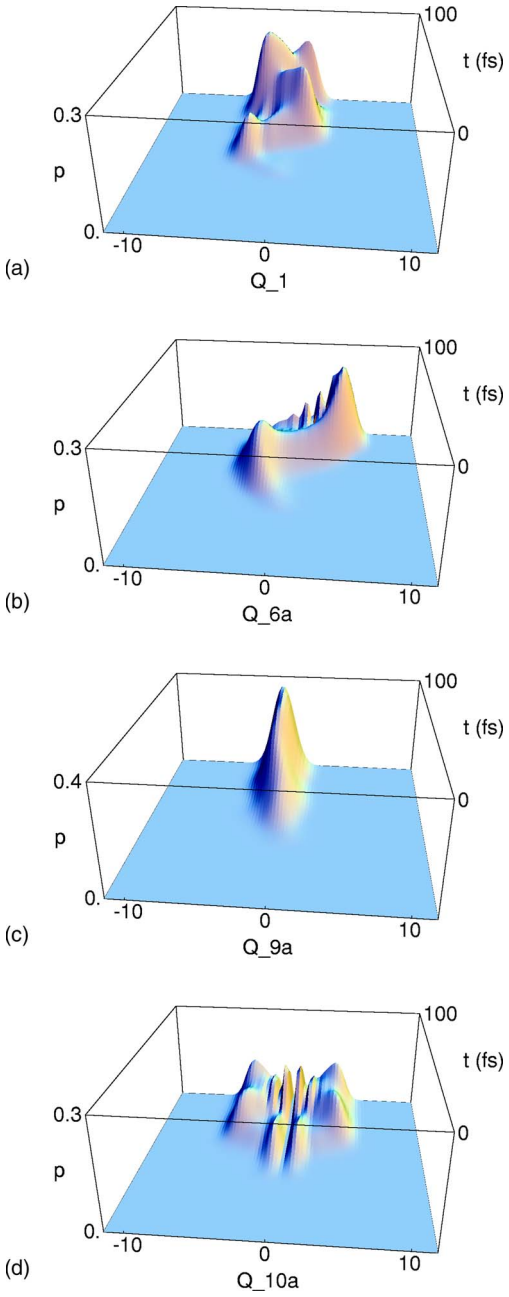

FIG. 13. Temporal evolution of the reduced S_1-state coordinate probability distributions using the four-mode model. The control task refers to that of the upper panel of Fig. 12. From the top to the bottom: mode 1, mode 6*a*, mode 9*a*, and mode 10*a*.

C. Acceleration of the S_2-S_1 internal conversion: Choice of different vibrational target states at the S_1 electronic state PES

To investigate laser pulse control of the IC process into the S_1 electronic state in more detail we proceed as in Sec. IV A and introduce target states as displaced vibrational ground states $\Pi_j \chi_{S_0,0}(Q_j - Q_j^{(\mathrm{tar})})$, where $Q_j^{(\mathrm{tar})}$ specifies the displacement of the vibrational wave function with respect to the particular coordinate. Noting the results displayed in Fig. 7 we realize that the wave packets of the two tuning modes move to their equilibrium position at final time.

Table II lists the results of simulations where the target wave packet was set at the tuning modes' equilibrium posi-

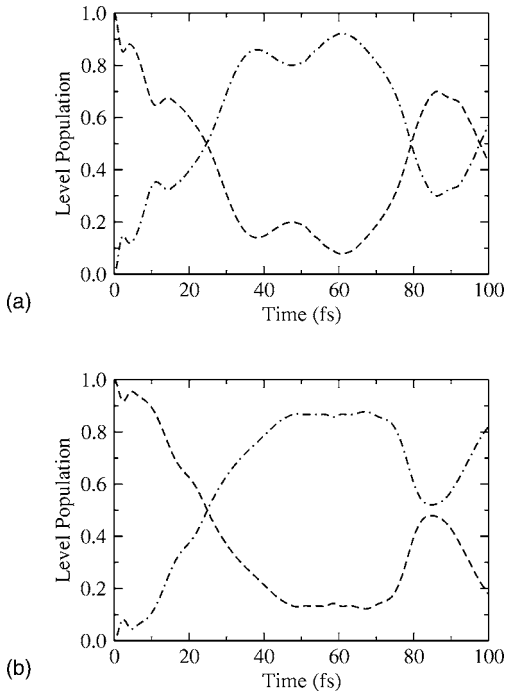

FIG. 14. Temporal evolution of the total population of the S_2 (dashed line) and S_1 states (dashed-dotted line) after an impulsive excitation of the S_2 state. Upper panel: three-mode model, lower panel: four-mode model.

tion in the S_1 or S_2 state (see Table I) and with respect to the coupling mode located either at 1.0 or 2.0. Additionally, our simulations indicate that a lower value of Λ_0 does not lead to a stable solution of the control task. Choosing a larger value and increasing the control pulse length via an increase of t_f increases somewhat the yield. The effect on the renormalized control yield $O(t_f)/P_a(t_f)$, however, is less pronounced. But the respective numbers somewhat below 0.4 show that the driven wave packet matches the target state to a sufficient extent. The related level populations are shown in Fig. 8. If one compares the coordinate probability distributions (not shown) with the behavior shown in Fig. 7 pronounced differences become obvious. There are no large oscillations with respect to the tuning modes. The wave packet gets its maximal value at the target state at the final time t_f. The coupling mode disperses symmetrically (formation of a hump shaped wave packet). It can be also seen in Fig. 8 that the optimal pulse covers the whole time interval. Although directly addressed in the optical excitation the population of the S_2 state is suppressed in the whole time interval. Notice that although Λ_0 has been taken five times larger than the value used in Fig. 6 the field strength does not change considerably.

To highlight the effect of IC in a somewhat different way we consider a control task where the target wave packet is located at the S_0-state PES (consideration of a pump-dump process) and at the S_1-state equilibrium position of the tuning modes (as listed in the fourth line of Table II). Figure 9 shows the level populations of this pump-dump process. Interestingly, the optimal pulse covers eight subpulses depopulating and repopulating the electronic ground state. In the whole excitation process the population of the S_2 state is

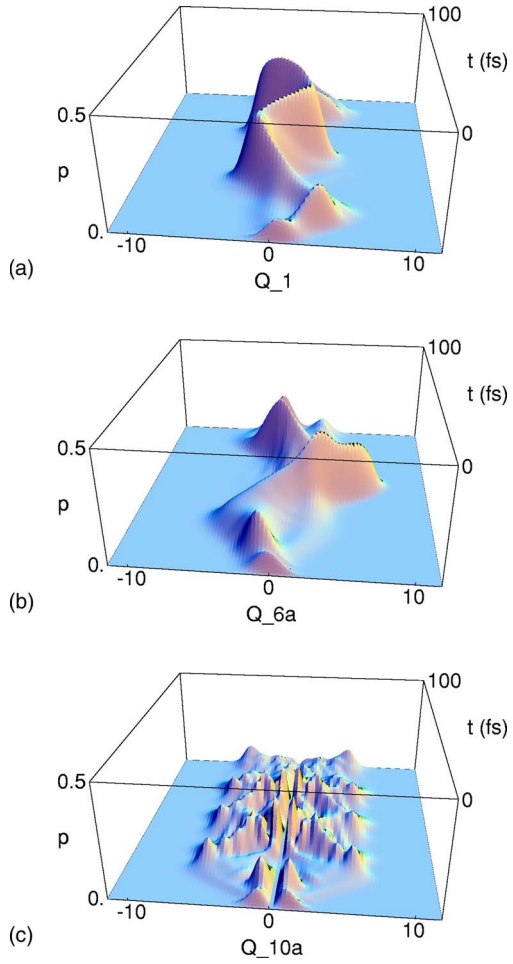

FIG. 15. Temporal evolution of the reduced S_1-state coordinate probability distributions after an impulsive excitation of the S_2 state and in using the three-mode model. From the top to the bottom: mode 1, mode 6a, and mode 10a.

small compared with that of the S_1 state. And the latter is depopulated at the end of the laser pulse, too, although not directly coupled to the ground state.

A population of the S_2 state can only be achieved when removing the time dependence of the control parameter $\lambda(t)$ [see Eq. (14)]. The respective data are also given in Table II and have been computed with the target wave packet to be located at the equilibrium position of the two tuning modes in the S_2 state $(Q_1^{(\mathrm{tar})}, Q_{6a}^{(\mathrm{tar})}, Q_{10a}^{(\mathrm{tar})}) = (2.02, -2.01, 1.0)$. Related state populations and coordinate probability distributions are presented in Figs. 10 and 11, respectively. Compared with the control task where the whole S_2 state has been taken as a target state the wave packet propagation is much more structured. The optimal pulse populates, depopulates, and repopulates the S_2 state to finally reach the target state at time t_f.

D. Application of the four-mode pyrazine model

In this last section we confront the computations presented so far with results obtained for a four-mode model of pyrazine.[16,33] Besides the two totally symmetric tuning modes $j=1, 6a$ and the coupling mode $j=10a$ it further includes the additional totally symmetric tuning mode $j=9a$. (As in the preceding considerations the remaining totally

symmetric modes which couple only weakly to the S_1 and S_2 states are omitted.) In the four-mode model the modes $j=6a$ and $j=9a$ are the Condon-active modes in the $n\rightarrow\pi^*$ excitation, while the modes $j=1$ and $j=6a$ are primarily Condon active in the $\pi\rightarrow\pi^*$ excitation. Note that the introduction of the additional tuning mode changes all parameters used within the three-mode model (see Table I) but, apparently, improves the simulation of the electron-vibrational dynamics of pyrazine.[16,33]

To be comparable to the computations discussed so far in the framework of the three-mode model we repeat the control tasks based on the target state which is either the overall S_1 or the S_2 state (see Figs. 12 and 13). When confronting the electronic level populations of the three-mode model (Fig. 6) with that of the four-mode model (Fig. 12) and the respective reduced coordinate probability distributions (Figs. 7 and 13), they are all rather similar. Also the shapes of the optimal pulses do not differ so much. There is a similar oscillation in the $j=1$ and $j=6a$ modes while the $j=9a$ mode does not show such pronounced oscillations. In the four-mode model, additionally, the dispersion of the coupling mode is less strong.

In order to clearly demonstrate the wave packet motion in each coordinate, we also calculated the expectation values, Eq. (23), of the various vibrational coordinates related to a particular electronic state (not shown). It is found that in the three-mode model the expectation values of Q_1 and Q_{9a} reach (after several oscillations) at final time their equilibrium positions ($Q_1^{(S_1)}=-0.37$, $Q_{9a}^{(S_1)}=-1.02$, see Table I). In contrast, that of the coordinate Q_{6a} stays at a value of about 1.7, which is somewhat away from its equilibrium position $Q_{6a}^{(S_1)}=1.3$. As already mentioned before the expectation value of the coupling mode remains at zero because of the symmetry of the whole IC process. For the four-mode model and in the considered time interval of 30 fs the tuning modes 1 and $9a$ get their equilibrium position, while the $6a$ mode just reaches $Q_{6a}=-0.5$ at the final time.

V. CONCLUSIONS

We demonstrated possible laser pulse control of molecular dynamics in multimode systems by combining optimal control theory (OCT) with the multiconfiguration time-dependent Hartree (MCTDH) method. This OCT-MCTDH approach has been exemplified for the well-established three- and four-mode three-electronic-level models of pyrazine. To explain the performance of the OCT-MCTDH approach we restricted our considerations on rather basic control tasks. They either aimed at a population maximization of one of the two excited states (showing vibronic coupling) or they tried to hit a particular wave packet in these states. In any case the control target should be reached at a particular time, which of course, represents an idealization of respective experiments. Nevertheless, differences of the driven dynamics to a free wave packet motion after ultrafast (impulsive) excitation into the S_2 state have been found mainly for the case where the target state is specified by a particular wave packet.

The strong vibronic coupling, however, introduces particular restrictions for the choice of the target state. It might be only useful to control wave packet formation in the lower lying S_1 excited state or to deform the electronic ground-state vibrational wave function within a pump-dump scheme.

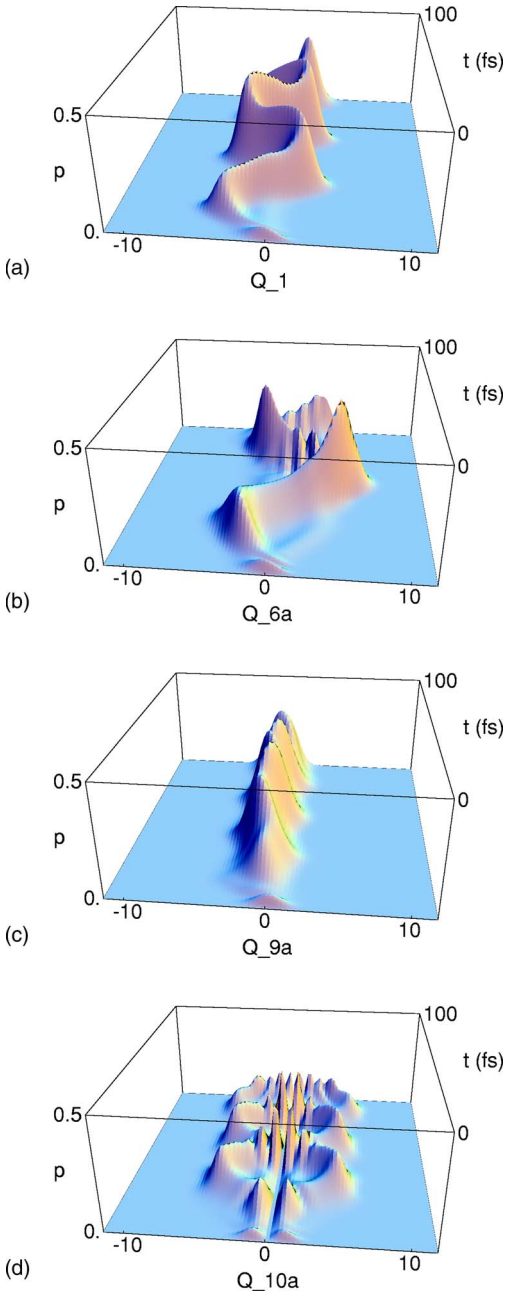

FIG. 16. Temporal evolution of the reduced S_1-state coordinate probability distributions after an impulsive excitation of the S_2 state and in using the four-mode model. From the top to the bottom: mode 1, mode $6a$, mode $9a$, and mode $10a$.

The results obtained within the described application of the combined OCT-MCTDH technique to the three- and four-mode vibronic coupling models of pyrazine with rather regular potential energy surfaces have to be considered as reference data. Laser pulse control of more involved dynamics is under work.

ACKNOWLEDGMENT

Financial support by the *Deutsche Forschungsgemeinschaft* through *Sonderforschungsbereich 450* is gratefully acknowledged.

TABLE III. Performance of OCT-MCTDH approach (the control task refers to the maximization of the S_1-state population at t_f=100 fs and described in the three-mode pyrazine model). Listed are ν=5 different sets of calculations (see text). Every one is ordered with respect to the vibrational modes j and characterized by a certain number M of single particle functions as well as particular natural populations (NP). Both numbers are ordered with respect to their electronic state contributions (S_0, S_1, and S_2 states—from the left to the right). The basic time step Δt (in fs) of the propagation as well as the performance (for the machine see text) given by the overall computational time T (in h) are also presented.

ν	j	M	NP	Δt	T
	1	8 7 8	1.514E−6 2.221E−3 6.881E−4		
1	6a	8 7 8	1.011E−6 1.862E−2 7.103E−3	0.04	27
	10a	8 7 8	1.115E−7 3.847E−3 5.989E−4		
	1	8 10 10	4.875E−6 3.677E−5 1.740E−5		
2	6a	8 12 12	3.428E−6 4.233E−3 1.781E−3	0.04	29
	10a	8 10 10	4.535E−7 2.725E−7 7.275E−7		
	1	8 10 10	6.256E−6 3.265E−5 1.431E−5		
3	6a	8 16 16	5.901E−6 2.935E−5 6.847E−5	0.04	47
	10a	8 10 10	1.020E−6 2.678E−7 6.760E−7		
	1	8 10 10	9.271E−6 3.641E−5 1.900E−5		
4	6a	8 12 12	4.015E−6 4.234E−3 1.790E−3	0.08	11.5
	10a	8 10 10	6.045E−7 7.626E−7 1.360E−6		
	1	8 10 10	3.965E−7 1.406E−4 6.388E−5		
5	6a	8 12 12	2.083E−7 8.700E−4 3.017E−4	0.02	102
	10a	8 10 10	2.525E−8 2.101E−6 4.254E−6		

APPENDIX A: UNDRIVEN WAVE PACKET DYNAMICS IN THE COUPLED S_2-S_1 STATES

The electron-vibrational dynamics in the excited states of pyrazine showing the S_2-S_1 conical intersection have been already studied in Refs. 15 and 18. In order to compare the laser pulse driven dynamics, as discussed in the main text, with the freely moving wave packet after impulsive excitation, the respective data are presented here using the three-mode and the four-mode vibronic coupling model and focusing on a time interval of 100 fs. Therefore, we assume a preparation of the S_2 diabatic state at t=0 in moving the ground-state vibrational wave function of the S_0 state vertically to the S_2 state PES. The time-dependent populations of the S_2 state as well as of the S_1 state are displayed in Fig. 14. The population of S_2 state exhibits an initial decay within the first 40 fs, indicating strong internal conversion. Afterwards, the (quasiperiodic) recurrences of the population continue up to few hundred femtoseconds.[15,18]

It is also instructive to demonstrate the temporal evolution of the reduced coordinate probability distributions in each coordinate. Figures 15 and 16 show the S_1-state probability distributions in the three-mode and four-mode models. It is seen that all the tuning modes oscillate around their equilibrium positions, followed by large irregular fluctuations. In contrast, the reduced probability of the coupling mode shows a broad and symmetric dispersion.

APPENDIX B: PERFORMANCE OF THE MCTDH METHOD

The subsequent discussion mainly concentrates on the achieved precision and on the convergence behavior of the combined OCT-MCTDH method. An important check in this respect is the determination of the appropriate number of single particle function [see Eq. (15)] which can be measured by the related so-called natural populations. Unfortunately, different quantities to be calculated have a different sensitivity to changes with respect to the particular MCTDH wave function representation. Hence, the natural populations do not provide a unique measure of the convergence.[13]

We took a closer look on a series of representative simulations using various sets of single particle functions as given in Table III. The corresponding control yields versus the number of iterations of the OCT equations are shown in Fig. 17. All the results demonstrate how sensitive the control yield depends on the used number of single particle functions. Because of the strong S_1-S_2 state coupling one needs more single particle functions when populating the S_1 state. And since the tuning mode 6a shows the strongest oscilla-

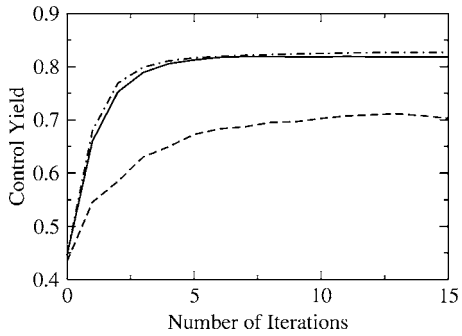

FIG. 17. Laser pulse driven maximization of the S_1-state population of pyrazine described in the three-mode model. The target state population is drawn vs the number of iterations of the OCT equations and for different sets ν of computations listed in Table III. Solid line: set ν=2 dashed-line: set ν=1 dashed-dotted line: set ν=3.

tions its simulation required the largest number of single particle functions. But enlarging their number increases the computational effort drastically, which is accumulated within the OCT iteration scheme. The difference with respect to the control yield between the sets 2 and 3 of computations represented in Table III is around 2%, but the computational time necessary for set 3 is about 1.5 times larger than that for set 2. Therefore, we consider the number of single particle functions used in set 2 to be sufficient. This set has been taken for all calculations discussed in the main part of the paper.

To find the appropriate step Δt in the time propagation the necessary precision has to be related to the available computer memory, since in the OCT scheme the complete coordinate dependence of the wave function (propagated forward as well as backward in time) has to be stored after each time step. For the calculations we chose $\Delta t=0.02$, 0.04, and 0.08 fs. The calculations using $\Delta t=0.04$ fs and 0.02 fs behave identically (convergence is reached after the 15th iteration). In the case of $\Delta t=0.08$ fs, however, the obtained optimal pulse is characterized by a number of abrupt changes indicating numerical instabilities. So we consider $\Delta t=0.04$ fs as the appropriate value for our simulations. The convergence of the control yield displayed in Fig. 17 also indicates the usefulness of the OCT iteration scheme suggested in Sec. III, although a strict proof of its behavior is not available.

It would be also of interest to test the necessary time needed for the computations (carried out with a 1 Gbyte memory and 1670 MHz frequency machine). We compared the MCTDH propagation done with a field of given time dependence and with a propagation which includes the computation of the field. Using $\Delta t=0.04$ fs and $t_f=100$ fs the first type of computations just needs 6 min for the three-mode model and 22 min for the four-mode model. Within the combination of the MCTDH propagation with the iteration scheme mentioned in Sec. III the program needs to read the forward and backward propagated wave functions at every time step and has to carry out the extrapolation for the field strength. Here, a single propagation up to $t=t_f$ needs 28 min when using the three-mode model and 80 min in the four-mode case.

[1] *Coherent Control of Photochemical and Photobiological Processes*, edited by J. L. Herek, special issue of J. Photochem. Photobio. (to be published).
[2] *Quantum Control of Light and Matter*, edited by Th. Halfmann, special issue of Opt. Commun. (to be published).
[3] J. L. Herek, W. Wohleben, R. J. Cogdell, D. Zeidler, and M. Motzkus, Nature (London) **417**, 533 (2002).
[4] D. Zeidler, S. Frey, W. Wohlleben, M. Motzkus, F. Busch, T. Chen, W. Kiefer, and A. Materny, J. Chem. Phys. **116**, 5231 (2002).
[5] T. Brixner, N. H. Damrauer, B. Kiefer, and G. Gerber, J. Chem. Phys. **118**, 3692 (2003).
[6] C. Daniel, J. Full, L. González, C. Lupulescu, J. Manz, A. Merli, S. Vajda, and L. Wöste, Science **299**, 536 (2003).
[7] G. Vogt, G. Krampert, P. Niklaus, P. Nuernberger, and G. Gerber, Phys. Rev. Lett. **94**, 068305 (2005).
[8] K. Sundermann and R. de Vivie-Riedle, J. Chem. Phys. **110**, 1896 (1999).
[9] M. Abe, Y. Ohtsuki, Y. Fujimura, and W. Domcke, J. Chem. Phys. **123**, 144508 (2005).
[10] L. Wang and V. May, J. Chem. Phys. **121**, 8039 (2004).
[11] H.-D. Meyer, U. Manthe, and L. S. Cederbaum, Chem. Phys. Lett. **165**, 73 (1990).
[12] U. Manthe, H.-D. Meyer, and L. S. Cederbaum, J. Chem. Phys. **97**, 3199 (1992).
[13] M. H. Beck, A. Jäckle, G. A. Worth, and H.-D. Meyer, Phys. Rep. **324**, 1 (2000).
[14] H. Köppel, W. Domcke, and L. S. Cederbaum, Adv. Chem. Phys. **57**, 59 (1984).
[15] R. Schneider, W. Domcke, and H. Köppel, J. Chem. Phys. **92**, 1045 (1990).
[16] L. Seidner, G. Stock, A. L. Sobolewski, and W. Domcke, J. Chem. Phys. **96**, 5298 (1992).
[17] A. Kühn and W. Domcke, J. Chem. Phys. **116**, 263 (2002).
[18] *Conical Intersections: Electronic Structure, Dynamics and Spectroscopy*, edited by W. Domcke, D. R. Yarkony, and H. Köppel (World Scientific, Singapore, 2004).
[19] G. A. Worth, H.-D. Meyer, and L. S. Cederbaum, J. Chem. Phys. **109**, 3518 (1998).
[20] G. A. Worth, H.-D. Meyer, and L. S. Cederbaum, J. Chem. Phys. **105**, 4412 (1996).
[21] H.-D. Meyer, J. Phys.: Conf. Ser. **4**, 66 (2005).
[22] S. A. Rice and M. Zhao, *Optical Control of Molecular Dynamics* (Wiley, New York, 2000).
[23] M. Shapiro and P. Brumer, *Principles of the Quantum Control of Molecular Processes* (Wiley, New Jersey, 2003).
[24] V. May and O. Kühn, *Charge and Energy Transfer Dynamics in Molecular Systems* (Wiley-VCH, Berlin, 2004).
[25] Y. J. Yan, R. E. Gillian, R. M. Whitnell, K. R. Wilson, and S. Mukamel, J. Phys. Chem. **97**, 2320 (1993).
[26] W. Zhu, J. Botina, and H. Rabitz, J. Chem. Phys. **108**, 1953 (1998).
[27] W. Zhu and H. Rabitz, J. Chem. Phys. **109**, 385 (1998).
[28] Y. Maday and G. Turinici, J. Chem. Phys. **118**, 8191 (2003).
[29] J. P. Palao and R. Kosloff, Phys. Rev. A **68**, 062308 (2003).
[30] G. A. Worth, M. Beck, A. Jäckle, and H.-D. Meyer, MCTDH package, Version 8.3, University of Heidelberg, Heidelberg, 2003.
[31] R. Schneider and W. Domcke, Chem. Phys. Lett. **150**, 235 (1988).
[32] G. Stock and M. Thoss, *Conical Intersections: Electronic Structure, Dynamics, and Spectroscopy* (Ref. 18), p. 619.
[33] C. Woywod, W. Domcke, A. L. Sobolewski, and H.-J. Werner, J. Chem. Phys. **100**, 1400 (1994).